Goldstone-like phonon modes in a (111)-strained perovskite

A. Marthinsen,[1] S. M. Griffin,[2,3] M. Moreau,[4] T. Grande,[1] T. Tybell,[4] and S. M. Selbach[1,*]

[1]*Department of Materials Science and Engineering, Norwegian University of Science and Technology (NTNU), 7491 Trondheim, Norway*
[2]*Molecular Foundry, Lawrence Berkeley National Laboratory, Berkeley, California 94720, USA*
[3]*Department of Physics, University of California, Berkeley, Berkeley, California 94720, USA*
[4]*Department of Electronic Systems, Norwegian University of Science and Technology (NTNU), 7491 Trondheim, Norway*

Goldstone modes are massless particles resulting from spontaneous symmetry breaking. Although such modes are found in elementary particle physics as well as in condensed-matter systems like superfluid helium, superconductors, and magnons, structural Goldstone modes are rare. Epitaxial strain in thin films can induce structures and properties not accessible in bulk and has been intensively studied for (001)-oriented perovskite oxides. Here we predict Goldstone-like phonon modes in (111)-strained $SrMnO_3$ by first-principles calculations. Under compressive strain the coupling between two in-plane rotational instabilities gives rise to a Mexican hat-shaped energy surface characteristic of a Goldstone mode. Conversely, large tensile strain induces in-plane polar instabilities with no directional preference, giving rise to a continuous polar ground state. Such phonon modes with $U(1)$ symmetry could emulate structural condensed-matter Higgs modes. The mass of this Higgs boson, given by the shape of the Mexican hat energy surface, can be tuned by strain through proper choice of substrate.

I. INTRODUCTION

Spontaneous symmetry breaking (SSB) spans the entire energy landscape of physics with manifestations ranging from high-energy particle collisions to low-temperature phase transitions in condensed matter [1]. When a continuous symmetry is spontaneously broken there exists a massless particle corresponding to a zero-frequency collective mode with continuous $U(1)$ symmetry, the so-called Mexican hat energy potential [2–4]. This is described by the Goldstone theorem, which has been studied in systems ranging from magnons [2] and liquid crystals [5] to Heisenberg ferromagnets [6] and incommensurate phases [7].

Another possible consequence of SSB is the formation of topological defects, which occur when the symmetry-breaking phase transition also results in a nontrivial change in the topology of the order parameter describing the phase transition. Depending on this topology change and the dimension of the system under consideration, these topological defects can be two-dimensional (2D) domain walls, one-dimensional (1D) vortices or "strings" and zero-dimensional (0D) monopoles [8]. Originally formulated to describe symmetry-breaking phase transitions in the early universe [9,10], several systems in condensed matter have been found to host topological defects, such as superfluid ^{4}He [11], high-temperature superconductors [12,13], and multiferroic h-RMnO$_3$ hexagonal manganites, with defect density predicted by the Kibble-Zurek mechanism [10,11].

Despite their abundance in other phases of matter, few examples of Goldstone modes in crystalline solids have been reported, e.g., artificial layered Ruddlesdon-Popper PbSr$_2$Ti$_2$O$_7$ [14], superconducting Cd$_2$Re$_2$O$_7$ [15,16], and 2D antiferro-

magnetic Ca$_2$RuO$_4$ [17]. Additionally, the h-RMnO$_3$ possess a disordered high-temperature phase with emergent $U(1)$ symmetry, characteristic of Goldstone modes [18–20].

Coherent epitaxial strain is a powerful way to enhance, control, and even induce new functionality, especially in perovskite oxides [21]. Well-known examples include enhanced polarization in BaTiO$_3$ [22], ferroelectricity in SrTiO$_3$ [23], and coexistence of metallic and insulating phases in perovskite manganites [24], as well as multiferroicity in EuTiO$_3$ [25] and SrMnO$_3$ [26]. While most perovskite thin films have been grown along the [001] direction, recent progress has enabled the exploration of a variety of symmetry constraints at oxide interfaces [27]. In particular, the symmetry and interactions across epitaxial (111) interfaces has led to novel phenomena like exchange bias in LaNiO$_3$-LaMnO$_3$ superlattices [28] and two-dimensional topological insulators [29].

Different crystallographic orientations can give rise to diverging interfacial coupling and resulting properties. Layer stacking sequences in the [111] and [001] directions in perovskites are -[B-AO_3]- and −[AO-BO_2]-, respectively, giving different interfacial coupling across epitaxial interfaces [30]. Strain in the (111) plane along octahedral faces yields a trigonal distortion of the BO$_6$ octahedra, with tensile and compressive strain inducing out-of-plane compression or elongation, respectively. In contrast, (001) strain parallel or perpendicular to BO bonds yields a tetragonal distortion, with different crystal field splitting and electronic structure compared to (111) strain [31].

Latent multiferroic SrMnO$_3$ lies at the stability edge between perovskite and 4H hexagonal polytype structure [32], and is hence susceptible to small perturbations which can drive phase transitions [32–36]. Bulk SrMnO$_3$ is a nonpolar G-type antiferromagnet [32], while (001) strain has been predicted [37] to induce both ferromagnetism and ferroelectricity, and the latter has been experimentally demonstrated [26]. While

*selbach@ntnu.no

dipoles in prototypical ferroelectrics like $BaTiO_3$ are stabilized by covalency between O $2p$ states and the formally empty d states of a d^0 B cation [38], the t_{2g} electrons of Mn^{4+} hinder such charge transfer in bulk $SrMnO_3$. However, by reducing electronic repulsions through lattice expansion, e.g., by strain or replacing Sr^{2+} with larger Ba^{2+}, charge transfer to the empty e_g states can occur, inducing multiferroicity by "directional d^0-ness" [39].

Here we predict both polar and nonpolar Goldstone-like modes in (111)-strained $SrMnO_3$ by first-principles electronic structure and lattice dynamics calculations and discuss the necessary structural and chemical factors stabilizing the Goldstone modes. The strain-induced SSB phase transitions can potentially host topological vortices. While excitations along the brim of the Mexican hat potential represent Goldstone modes, excitations from the brim to the top of the hat correspond to Higgs modes, and we address the possibility of controlling the Higgs excitation mass by epitaxial strain.

II. COMPUTATIONAL DETAILS

Calculations were performed using the VASP [40] code with the PBEsol [41] functional and a Hubbard U correction of 3 eV applied to the Mn $3d$ orbitals [42]. Plane waves were expanded up to a kinetic energy cutoff of 650 eV and sampled with a Γ-centered $6 \times 6 \times 2$ mesh for hexagonal 30-atom cells and a Γ-centered $4 \times 4 \times 4$ mesh for pseudocubic 40-atom cells. Projector augmented wave (PAW) potentials [43] treated Sr $(4s^2 4p^6 5s^2)$, Mn $(3p^6 4s^2 3d^5)$, and O $(s^2 p^4)$ states as explicit valence electrons. Atomic positions were relaxed until forces on all ions were below 1 meV/Å. Phonon calculations were carried out on high-symmetry ($R\bar{3}m$ structures and $P4/mmm$ structures for (111) and (001) strain, respectively) 40-atom pseudocubic structures, obtained by rotation of relaxed hexagonal cells for each strain. G-type antiferromagnetic ordering was enforced throughout the phonon calculations. The software PHONOPY [44] was used for the phonon calculations, and FINDSYM [45] was used to determine the space groups with a tolerance on the atomic positions equal to 10^{-3} Å. The Berry-phase formalism was used to evaluate the electronic contribution to the ferroelectric polarization [46,47].

III. LATTICE INSTABILITIES AND NOTATION

We first address the effect of epitaxial strain on structural instabilities in the high-symmetry structures ($R\bar{3}m$ for (111) strain and $P4/mmm$ for (001) strain) using density functional theory (DFT) calculations. For octahedral rotations we let α, β, and γ [Fig. 1(a)] denote rotation about the pseudocubic axes, x, y, and z, respectively, while α', β', and γ' denote rotation about the orthogonal axes along the pseudocubic vectors $[1\bar{1}0]$, $[11\bar{2}]$, and $[111]$, respectively [Fig. 1(b)], where the two former lie in the (111) plane. The rotational amplitudes α, β, and γ about pseudocubic [100], [010], and [001] axes for any chosen rotational vector are proportional to its vector elements, so that, e.g., rotations about the $[1\bar{1}0]$ rotational axis result in rotations $\alpha = \beta$, $\gamma = 0$, and rotations about $[11\bar{2}]$ result in rotations $\gamma = 2\alpha = 2\beta$. Out-of-phase rotational modes are favored over in-phase modes for all considered strain values, as shown in Fig. 1(c). $SrMnO_3$ is predicted to have three degenerate rotational instabilities also with 0% strain at 0 K, giving an
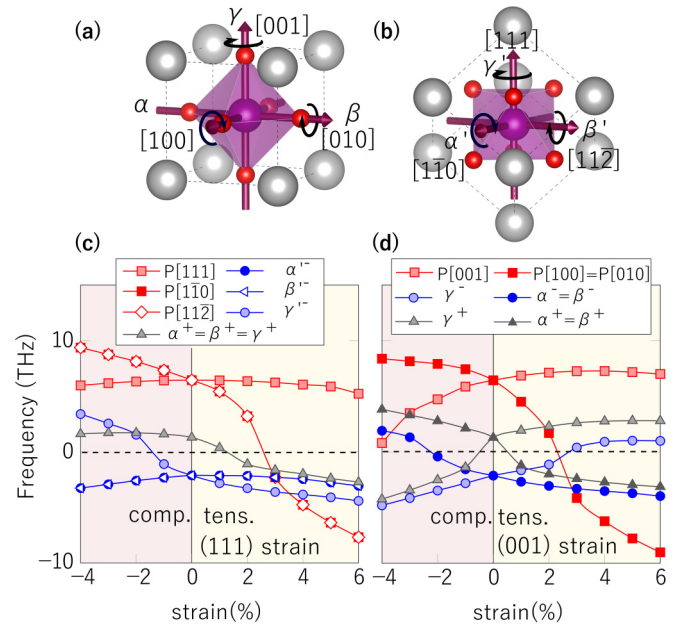

FIG. 1. Evolution of structural instabilities in $R\bar{3}m$ and $P4/mmm$ $SrMnO_3$ under (111) and (001) epitaxial strain, respectively. (a) Visualization of the pseudocubic [100], [010], and [001] axes. Octahedral rotations about the respective axes are denoted α, β, and γ. (b) Visualization of the pseudocubic $[1\bar{1}0]$, $[11\bar{2}]$, and [111] axes, where the two former lie in the (111) plane. Octahedral rotations about the $[1\bar{1}0]$, $[11\bar{2}]$, and [111] axes are labeled α', β', and γ', respectively. Evolution of rotational and polar modes with c) (111) and d) (001) epitaxial strain. Polar modes are shown in red, out-of-phase rotations ($^-$) are blue, and in-phase rotations ($^+$) are gray.

$R\bar{3}c$ structural ground state with an octahedral rotation angle of 2.4°, and is 3.7 meV/f.u. lower in energy than the cubic aristotype structure. A rhombohedral ground state has not been observed experimentally [48], but our predicted structural distortion would give a very subtle experimental signature, and the modest octahedral tilting could easily be rectified by the presence of oxygen vacancies. The degeneracy of the rotational modes is lifted under (111) strain, and the out-of-phase modes are split into one rotational mode about the [111] out-of-plane axis and two rotational modes about the $[11\bar{2}]$ and $[1\bar{1}0]$ in-plane axes [31]. Although the $[11\bar{2}]$ direction, pointing towards an octahedral face, and the $[1\bar{1}0]$ direction, pointing towards an octahedral edge, are *not* symmetry equivalent, the rotational modes about these axes are degenerate under all considered strain values. We find that compression favors in-plane rotations over out-of-plane ones, which are stabilized at about -1% strain, whereas tensile strain favors out-of-plane rotations. To illustrate the different structural response to (111) strain compared with (001) strain, we show the evolution of rotational and polar phonon modes under (001) strain [49] [Fig. 1(d)]. The splitting of rotational out-of-phase modes into one out-of-plane mode and two degenerate in-plane modes is analogous to (111) strain, but with the opposite response. Suppression of out-of-plane polarization under (111) compressive strain is geometrically driven since the three oxygens in the AO_3 layers are pushed together, hindering Mn displacement [50,51]. Under compressive (001) strain the Poisson elongation of the out-of-plane octahedral axis allows the displacement of Mn.
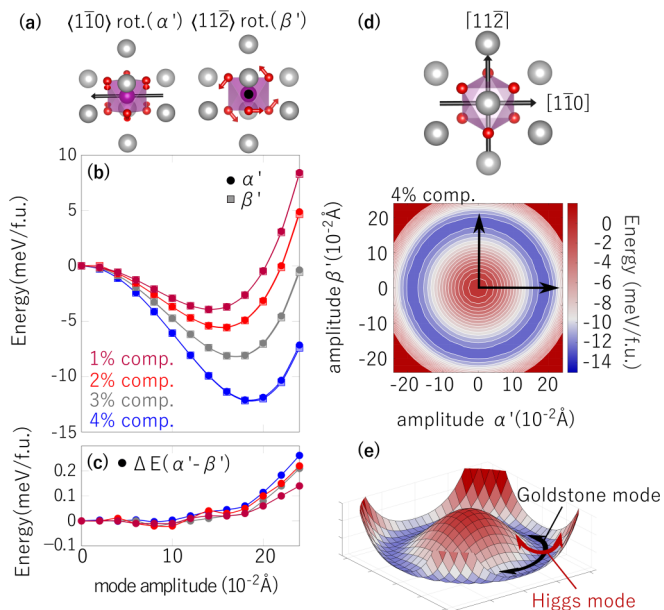
FIG. 2. Energy landscape of rotational phonon modes in SrMnO$_3$ under compressive (111) strain. (a) Atomic displacements corresponding to the two in-plane rotational modes, α' and β'. (b) Energy landscape α' and β' modes distorted from the high-symmetry $R\bar{3}m$ phase, shown for compressive strain values between 1% and 4%. (c) Energy difference between α' and β' modes showing an increased preference for the β' mode with increasing amplitude. (d) Coupling of the two in-plane rotational modes at 4% compressive strain, resulting in a rotationally invariant energy landscape: a Mexican hat potential. Directions in the Mexican hat potential directly translate to in-plane rotational axes, as illustrated in the upper panel. The arrows indicate orthogonal in-plane rotational axes corresponding to the [11$\bar{2}$] and [1$\bar{1}$0] axes. (e) Illustration of a Goldstone mode in which there can be massless excitations to new distinct phases along the brim of the Mexican hat.

IV. EPITAXIAL-STRAIN-INDUCED GOLDSTONE-LIKE MODES

A. Compressive strain

We now consider the energy landscape of the two in-plane rotational modes (α' and β') [Fig. 2(a)] under compressive (111) strain, showing the energy lowering from $R\bar{3}m$ as a function of mode amplitude in Fig. 2(b). Both the energy-minimizing mode amplitude and the energy lowering increases with increasing compressive (111) strain, implying that SrO$_{12}$ dodecahedra are more compressible than MnO$_6$ octahedra under (111) strain. Condensation of the α' and β' modes results in equally energy-lowering structures within the energy resolution of our calculations, even though the condensation of these modes yields different space groups and different resulting bond lengths. Under 2% and 4% compressive strain the rotational modes are stabilized by 6 and 12 meV/f.u. with respect to the $R\bar{3}m$ phase, respectively.

Due to the sixfold inversion axis (S_6), there are six symmetry-equivalent crystallographic directions within the $\langle 11\bar{2} \rangle$ and the $\langle 1\bar{1}0 \rangle$ family, respectively. Since octahedral rotation about either of these axes is equally energy lowering within our considered strain range, we get a total of 12

degenerate energy minima. The coupling between the α' and β' rotational modes is very weak, yielding an energy surface with a Mexican hat shape, where the ground state depends only on the distortion amplitude $\propto \alpha'^2 + \beta'^2$ (or $\alpha^2 + \beta^2 + \gamma^2$), and not the direction of the in-plane rotational axis, as shown in Fig. 2(d). In contrast, under (001) strain the coupling between the in-plane rotational modes α_{100} and β_{010} gives a distinct energy minimum along the [110] direction (see Fig. S1 of the Supplemental Material [52]).

A continuous degeneracy along the brim of a Mexican hat potential with $U(1)$ symmetry further implies a continuous set of degenerate structures described as a Goldstone-like mode with zero energy barrier to undergo a transition to a new phase with a different in-plane rotational axis [Fig. 2(e)]. Importantly, the rotation mode amplitude *increases* with increasing (111) compressive strain for SrMnO$_3$, unlike LaAlO$_3$ where the amplitude decreases due to the different polyhedral compressibilities [31]. Compressive strain can thus serve as a control parameter to tune the rotational mode amplitude in SrMnO$_3$ and consequently the shape of the Mexican hat potential, as discussed further below. However, the different symmetries of the α' and β' modes are increasingly reflected in diverging total energies as the mode amplitude increases under strain. The energy difference between the α' and β' rotational modes as a function of mode amplitude in Fig. 2(c) shows that for increasing amplitudes a preference for β' develops. This implies that under sufficiently large mode amplitude, for compressive strains larger than our calculated 4%, the degeneracy of the in-plane rotational axes is lifted, giving six energy minima in the brim of the Mexican hat energy potential. Therefore, a further symmetry-breaking phase transition from a $U(1)$ to a Z_6 state will occur with increasing mode amplitude upon increasing strain, analogous to the ferroelectric transition in h-RMnO$_3$, which displays the same emergent $U(1)$ symmetry [53]. We note that the h-RMnO$_3$ lie on the opposite stability edge with respect to the Goldschmidt tolerance factor compared to SrMnO$_3$.

B. Tensile strain

We now turn to *tensile* strain and find that the in-plane rotational modes α' and β' are also imaginary, but suppressed by the out-of-plane γ' mode. However, tensile strain also induces two orthogonal in-plane ferroelectric instabilities where Mn is displaced along the [1$\bar{1}$0] and [11$\bar{2}$] axes, respectively [Fig. 1(c)]. These polar modes become unstable at $\sim$2.5% strain, but competition with the rotational γ' mode suppresses them up to 4% strain. The out-of-plane polar mode along [111] is insensitive to (111) strain, and remains stable under both compressive and tensile strain. In contrast, (001) strain softens ferroelectric modes both under compression, **P** $\parallel$ [001], as well as tension, **P** $\parallel$ [100] and **P** $\parallel$ [010] [49].

We compare the energy lowering of the two orthogonal in-plane polar modes and the competing γ' mode [shown in Fig. 3(c)] from the high-symmetry $R\bar{3}m$ phase for tensile (111) strain ranging from 4% to 6% in Fig. 3(a). The two polar modes, each having six symmetry-equivalent crystallographic directions, reduce the crystal symmetry from $R\bar{3}m$ to $C2$ (**P**[1$\bar{1}$0]) and Cm (**P**[11$\bar{2}$]), respectively, when disregarding additional rotation. Analogous to the behavior of the in-plane
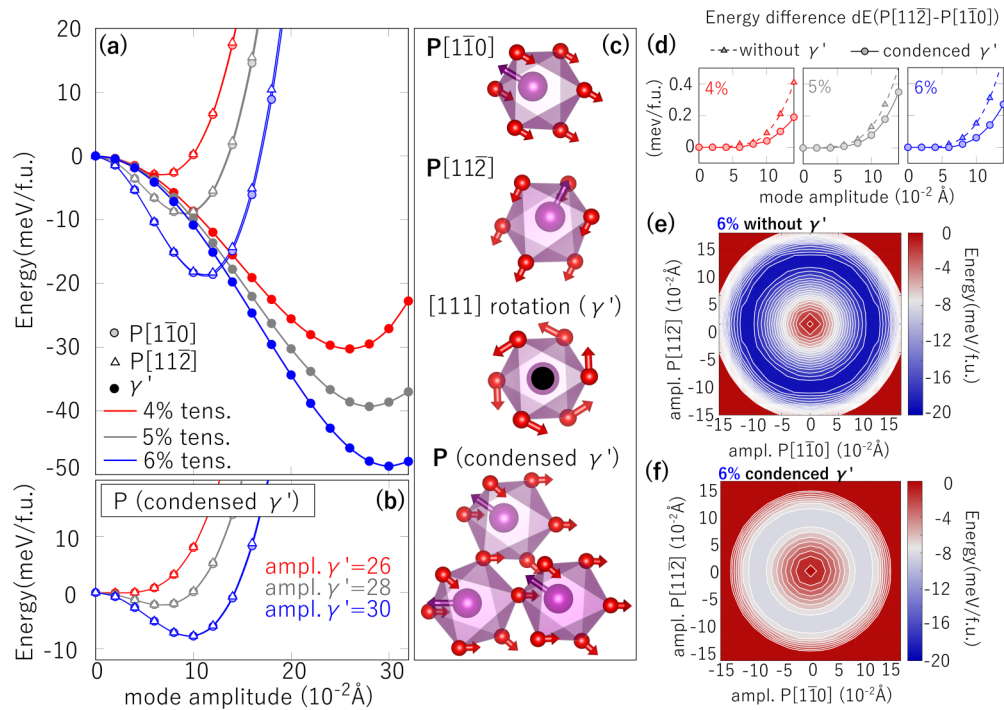
FIG. 3. Energy landscape of competing rotational and polar phonon modes in SrMnO$_3$ under tensile (111) strain. (a) Energy landscape of the rotational γ' and the two orthogonal polar modes P[1$\bar{1}$0] and P[11$\bar{2}$], distorted from the high-symmetry $R\bar{3}m$ phase, for tensile strains ranging from 4% to 6%. (b) The energy landscape of polar modes when the energy-minimizing rotational amplitude for each strain value is condensed. Condensed rotational amplitudes for the different strain values are indicated (red, 4%; gray, 5%; and blue, 6%). (c) Atomic displacements corresponding to the γ' mode, the polar P[11$\bar{2}$] and P[1$\bar{1}$0] (three upper panels), and resulting polarization behavior when the γ' mode is condensed (lower panel), in which atoms are no longer displaced along a single axis. (d) The energy difference for increasing mode amplitude between the polar direction P $\parallel$ [11$\bar{2}$] and P $\parallel$ [1$\bar{1}$0], indicating an increased preference for polarization along the [1$\bar{1}$0] direction. Dashed lines show the energy difference in the absence of rotations, whereas solid lines show the resulting reduced energy difference when the γ' mode is condensed. Energy landscape upon coupling the in-plane polar modes at 6% tensile strain resulting in a Mexican hat potential energy surface with rotationally invariant ground state both (e) in the absence of rotations and (f) in the presence of rotations frozen in the lowest-energy amplitude.

rotational modes under compressive strain, the two polar directions are equally energy lowering with minima differering by ∼0.1 meV/f.u. at 4% and ∼0.3 meV at 6% strain. However, the energy lowering from the in-plane polar modes is weaker than for the γ' rotational mode, even though the imaginary frequency is lower [Fig. 1(c)]. The effect of the rotational mode on the energy landscape along the two polar modes is assessed by freezing in the lowest-energy rotational amplitude and recalculating the energy landscape of the polar distortions [Fig. 3(b)]. Condensation of the γ' mode does not lift the degeneracy of the two orthogonal polar modes, as there is no out-of-plane displacement of oxygen under γ' rotation. However, the γ' mode suppresses the energy lowering and amplitude of the orthogonal polar modes. Under 5% and 6% tensile strain, the polar modes retain a finite amplitude under competition with the γ' rotational mode, whereas under 4% strain they are suppressed.

The energy difference between polar off-centering along the [11$\bar{2}$] and the [1$\bar{1}$0] directions increases with off-centering amplitude, progressively favoring displacements along [1$\bar{1}$0], as shown in Fig. 3(d). When the rotational γ' mode is included, the energy difference between polar off-centering in the two respective directions diminishes due to the reduced symmetry. In the presence of out-of-phase rotations, Mn offsets

in consecutive oxygen octahedra are no longer equivalent as they displace towards an octahedral face or edge; hence out-of-phase rotations favor in-plane isotropy between the two polar directions.

The coupling of the two polar modes is visualized for 6% strain in Figs. 3(e) and 3(f), in the absence of rotations [Fig. 3(e)], and in the presence of rotations frozen with their lowest-energy amplitude [Fig. 3(f)]. As also observed for in-plane rotational modes under compressive strain, there is no directional preference for in-plane polarization under (111) tensile strain, with less than 0.5 meV/f.u. variation along the brim of the Mexican hat potential, resulting in polar Goldstone-like modes.

V. MICROSCOPIC ORIGINS OF GOLDSTONE-LIKE MODES

We now discuss the origin of both the *nonpolar* Goldstone-like rotational mode under compression as well as the *polar* Goldstone-like modes under tensile strain. First we discuss the Goldstone-like rotational modes. Importantly, upon coherent (111) strain, all Mn-O bonds are equally elastically strained in the absence of rotations, and for any given in-plane rotational axis *all* Mn-O bonds will be altered to some degree
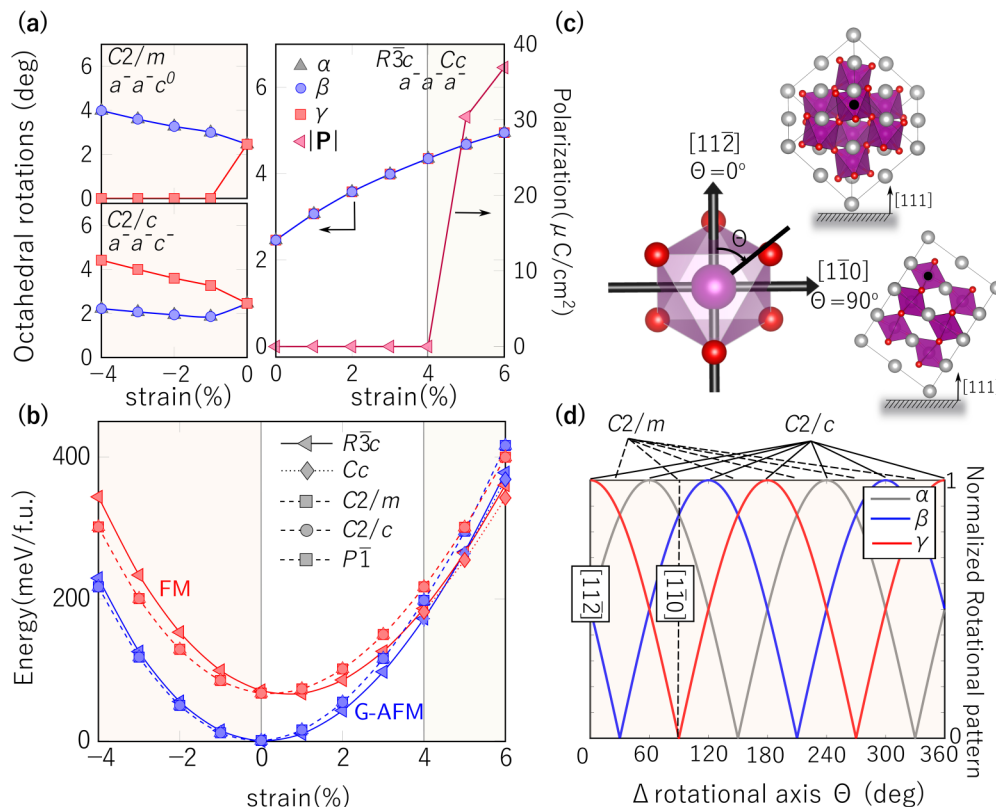
FIG. 4. Structural and magnetic phases in $SrMnO_3$ under (111) epitaxial strain. (a) Pseudocubic rotational angles and polarization as function of strain. Under compressive strain the $C2/c$ phase and the $C2/m$ phase are degenerate. (b) Total energy as a function of strain for different structural phases, comparing the stability of G-AFM ordering with FM ordering. Energies are given per formula unit with the $R\bar{3}c$ unstrained G-AFM structure as the reference state. A magnetic crossover from G-AFM to FM is found at ~4.5% tensile (111) strain. (c) Definition of the shift θ in in-plane rotational axis. $\theta = 0$ corresponds to the rotational axis [11$\bar{2}$], and $\theta = 90$ corresponds to the [1$\bar{1}$0] direction. (d) The analytically derived relation between the rotational angles α, β, and γ upon a shift (θ) of the in-plane rotational axis. Total rotational angles are normalized.

(Fig. S9 [52]) leading to small differences between α' and β' and weak coupling between the two modes. At moderate mode amplitudes, differences between in-plane rotational axes are thereby small, giving rise to a Goldstone-like nonpolar phonon mode. In contrast, under (001) strain the two in-plane rotational modes α and β only affect four out of six Mn-O bonds (Fig. S10 [52]), leading to an energetically favorable coupling between the two modes to distribute the strain over all six Mn-O bonds, giving rise to four distinct minima. Decomposition of the total energy into a band-energy contribution and an electrostatic-energy contribution (Fig. S3 [52]) shows that the α' and β' modes have almost identical impact on the two energy contributions for all compressive strains. Additionally, the band energy, which is increasingly lowered by larger rotations, dominates the total energy, accounting for the increased stabilization of rotations with compressive strain.

The polar Goldstone-like mode is stabilized by both structural and electronic factors. With alternating layers of AO_3 and B units along the [111] direction, there are no oxygen ions in the Mn displacement plane. Partial covalent bonds between empty Mn e_g states and O $2p$ states are thus weaker than under (001) strain where Mn is displaced directly towards an oxygen ion. We highlight the importance of the electronic structure of $SrMnO_3$ for stabilizing polar Goldstone-like modes by comparing with (111)-tensile-strained $BaTiO_3$, where an out-

of-plane polar component is predicted [51], precluding a rotationally invariant polar mode. However, when this out-of-plane polar mode remains stable, the coupling of the two in-plane polar modes in $BaTiO_3$ yields the same rotationally invariant in-plane polar mode (Fig. S4 [52]) as for $SrMnO_3$. This implies that only in the absence of an unstable out-of-plane polar mode can an in-plane polar Goldstone-like mode be realized in (111)-strained perovskites. While Ti^{4+} is a d^0 cation, the t_{2g} electrons of the d^3 Mn^{4+} cation prevents out-of-plane polar displacements of Mn, and concomitantly an unstable out-of-plane polar mode. While out-of-plane polar modes in $PbSr_2Ti_2O_7$ [14] are stabilized by confining the $6s^2$ lone-pair Pb^{2+} cations into single layers between nonpolar rock salt layers, out-of-plane modes in (111)-strained $SrMnO_3$ are stabilized by Mn^{4+} with d^3 configuration inherent in the material.

VI. PHASE DIAGRAM

The equilibrium structures under (111) strain are summarized in the phase diagram presented in Fig. 4(a) along with rotational distortions projected onto pseudocubic axes, and with the magnetic ground state shown in Fig. 4(b). G-type antiferromagnetism (G-AFM) is stabilized under compressive strain, while tensile strain progressively favors ferromagnetic order, which becomes stable at ~4.5%. The structural dif-

ferences between G-AFM and ferromagnetic (FM) SrMnO$_3$ are subtle and quantitative; we thus present the structural parameters calculated with G-AFM throughout the whole strain range for consistency. Condensation of the γ' mode results in a stable $a^-a^-a^-$ $R\bar{3}c$ structure which prevails up to 4% tensile strain, with octahedral rotations increasing with strain [Fig. 4(a)]. The increased octahedral rotations with tensile strain, progressively straining the Mn-O bonds, imply that the Sr-O bonds are mitigated, meaning that the SrO$_{12}$ dodecahedra are more rigid under (111) strain than the MnO$_6$ octahedra. This is analogous to the calculated isostatic strain behavior where octahedral rotations also increase with negative hydrostatic pressure (Fig. S11 [52]). Above 4% strain a polar Cc structure is stabilized, with a polarization of 36.9 μC/cm^2 at 6% strain.

Condensation of the rotational α' mode under compressive strain results in a monoclinic $a^-a^-c^\circ$ $C2/m$ structure, while condensation of β' gives a monoclinic $a^-a^-c^-$ $C2/c$ structure [Fig. 4(a)], which is degenerate within 1 meV/f.u., up to 4% strain. The symmetry equivalent $\langle11\bar{2}\rangle$ and $\langle1\bar{1}0\rangle$ axes are each separated by 60°; hence there are six symmetry-equivalent structures with space groups $C2/c$ and $C2/m$, respectively. All structures with a combination of in-plane $\langle11\bar{2}\rangle$ and $\langle1\bar{1}0\rangle$ rotation axes are identified as $a^-b^-c^-$ $P\bar{1}$. The pseudocubic rotational amplitudes α, β, and γ are related for a continuous set of energy-minimizing structures by the following equations [Fig. 4(d)]: $\alpha = -\frac{1}{2}(\sqrt{3}\sin(\theta) + \cos(\theta))$, $\beta = \frac{1}{2}(\sqrt{3}\sin(\theta) - \cos(\theta))$, and $\gamma = \cos\theta$, where θ is the shift of in-plane rotational axis as defined in Fig. 4(c).

VII. DISCUSSION AND CONCLUSION

Having established the structural, electronic, and chemical factors responsible for stabilizing Goldstone-like modes in (111)-strained SrMnO$_3$, we turn to the exotic physics of having such an emergent symmetry in perovskite oxides. Goldstone mode excitations around the brim of the Mexican hat (the azimuthal direction) imply a continuous change of phase, in this case corresponding to a degenerate rotation or polarization axis. In contrast to this, excitations up the brim, corresponding to a change in mode amplitude, are called Higgs modes [54,55]. Since these modes have a finite excitation gap—depending on the curvature of the energy potential—the Higgs modes are massive. From our detailed analysis of the role of strain in the energy landscape, we show that the shape of the Mexican hat potential can be tuned with epitaxial strain. Therefore, in our case, the mass of a Higgs mode can be tuned in (111)-strained SrMnO$_3$ by the choice of substrate. Under sufficiently large strain, compressive or tensile, the $U(1)$ symmetry of the Mexican hat will be broken and Z_6 symmetry with six local minima will emerge, in analogy with the hexagonal manganites [53].

The SSB in these strain-induced phase transitions is expected to result in one-dimensional topological vortices whose

quantity can be described by the Kibble-Zurek mechanism [10,11]. The first homotopy group of the order parameter space $U(1)$ is nontrivial, predicting the formation of vortices in SrMnO$_3$. Under compressive strain the order parameter is the orientation of the in-plane octahedral rotation axis, whereas under larger tensile strain the order parameter is the polarization vector. These vary continuously around the brim of the Mexican hat, analogous to the phase in superfluid He [11] and superconductors [56,57], the tilt angle in the hexagonal manganites [11,12,18–20], and the orientation in nematic liquid crystals [5]. The anticipated structural vortices in (111)-strained SrMnO$_3$ represent the high-symmetry phases on top of the Mexican hat: $R\bar{3}m$ and $R\bar{3}c$ under compressive and large tensile strain, respectively.

In contrast with liquid crystals, liquid ^{4}He, or superconductors, the Goldstone modes, Higgs modes, and vortices can be engineered by choice of substrate in epitaxially strained SrMnO$_3$. Substrates should be (111)-oriented cubic or rhombohedral to avoid nonquadratic biaxial strain which could break the symmetry of the Mexican hat potentials. A short discussion of possible substrates and the stability of SrMnO$_3$ towards oxygen vacancy formation is provided in the Supplemental Material. The effect of substrate interactions on octahedral rotations have been found by DFT to vanish 15 Å from the substrate, leaving a regime with strain effects [30,58]. We propose that the polar Goldstone modes under tensile strain could possibly be detected by Raman spectroscopy [15]. To detect nonpolar Goldstone modes under compressive strain, experimental probes sensitive to acoustic modes are required, e.g., inelastic neutron scattering [59].

In summary, we have mapped out the (111) epitaxial phase diagram for SrMnO$_3$ and established the main strain-mediating mechanisms. Compressive strain gives rise to nonpolar Goldstone-like modes, whereas large tensile strain induces a continuous polar ground state and polar Goldstone-like modes. SrMnO$_3$ is a potential condensed-matter system for studying the proliferation of topological vortices in the solid state, and for tuning the amplitudes of Goldstone and Higgs modes by epitaxial strain.

[1] H. Arodz, J. Dziarmaga, and W. H. Zurek, *Patterns of Symmetry Breaking* (Springer, Dordrecht, Netherlands, 2012).

[2] T. Schneider and P. F. Meier, Physica **67**, 521 (1973).

[3] J. Goldstone, Nuovo Cim. **19**, 154 (1961).

[4] J. Goldstone, A. Salam, and S. Weinberg, Phys. Rev. **127**, 965 (1962).

[5] I. Muševič, R. Blinc, and B. Žekš, *The Physics of Ferroelectric and Antiferroelectric Liquid Crystals* (World Scientific, Singapore, 2000).

[6] R. V Lange, Phys. Rev. **146**, 301 (1966).

[7] A. D. Bruce and R. A. Cowley, J. Phys. C Solid State Phys. **11**, 3609 (1978).

[8] S. M. Griffin and N. A. Spaldin, J. Phys. Condens. Matter **29**, 343001 (2017).

[9] T. W. B. Kibble, Phys. Today **60**, 47 (2007).

[10] T. W. B. Kibble, J. Phys. A. Math. Gen. **9**, 1387 (1976).

[11] W. H. Zurek, Nature (London) **317**, 505 (1985).

[12] A. K. Nguyen and A. Sudbø, Phys. Rev. B **57**, 3123 (1998).

[13] M. Kiometzis, H. Kleinert, and A. M. J. Schakel, Phys. Rev. Lett. **73**, 1975 (1994).

[14] S. M. Nakhmanson and I. Naumov, Phys. Rev. Lett. **104**, 097601 (2010).

[15] C. A. Kendziora, I. A. Sergienko, R. Jin, J. He, V. Keppens, B. C. Sales, and D. Mandrus, Phys. Rev. Lett. **95**, 125503 (2005).

[16] J. C. Petersen, M. D. Caswell, J. S. Dodge, I. A. Sergienko, J. He, R. Jin, and D. Mandrus, Nat. Phys. **2**, 605 (2006).

[17] A. Jain, M. Krautloher, J. Porras, G. H. Ryu, D. P. Chen, D. L. Abernathy, J. T. Park, A. Ivanov, J. Chaloupka, G. Khaliullin, B. Keimer, and B. J. Kim, Nat. Phys. **13**, 633 (2017).

[18] M. Lilienblum, T. Lottermoser, S. Manz, S. M. Selbach, A. Cano, and M. Fiebig, Nat. Phys. **11**, 1070 (2015).

[19] S.-Z. Lin, X. Wang, Y. Kamiya, G.-W. Chern, F. Fan, D. Fan, B. Casas, Y. Liu, V. Kiryukhin, W. H. Zurek, C. D. Batista, and S.-W. Cheong, Nat. Phys. **10**, 970 (2014).

[20] F.-T. Huang, X. Wang, S. M. Griffin, Y. Kumagai, O. Gindele, M.-W. Chu, Y. Horibe, N. A. Spaldin, and S.-W. Cheong, Phys. Rev. Lett. **113**, 267602 (2014).

[21] J. M. Rondinelli and N. A. Spaldin, Adv. Mater. **23**, 3363 (2011).

[22] K. J. Choi, M. Biegalski, Y. L. Li, A. Sharan, J. Schubert, R. Uecker, P. Reiche, Y. B. Chen, X. Q. Pan, V. Gopalan, L.-Q. Chen, D. G. Schlom, and C. B. Eom, Science **306**, 1005 (2004).

[23] J. H. Haeni, P. Irvin, W. Chang, R. Uecker, P. Reiche, Y. L. Li, S. Choudhury, W. Tian, M. E. Hawley, B. Craigo, A. K. Tagantsev, X. Q. Pan, S. K. Streiffer, L. Q. Chen, S. W. Kirchoefer, J. Levy, and D. G. Schlom, Nature (London) **430**, 758 (2004).

[24] K. H. Ahn, T. Lookman, and A. R. Bishop, Nature (London) **428**, 401 (2004).

[25] J. H. Lee, L. Fang, E. Vlahos, X. Ke, Y. W. Jung, L. F. Kourkoutis, J.-W. Kim, P. J. Ryan, T. Heeg, M. Roeckerath, V. Goian, M. Bernhagen, R. Uecker, P. C. Hammel, K. M. Rabe, S. Kamba, J. Schubert, J. W. Freeland, D. A. Muller, C. J. Fennie, P. Schiffer, V. Gopalan, E. Johnston-Halperin, and D. G. Schlom, Nature (London) **466**, 954 (2010).

[26] C. Becher, L. Maurel, U. Aschauer, M. Lilienblum, C. Magén, D. Meier, E. Langenberg, M. Trassin, J. Blasco, I. P. Krug, P. A. Algarabel, N. A. Spaldin, J. A. Pardo, and M. Fiebig, Nat. Nanotechnol. **10**, 661 (2015).

[27] H. Y. Hwang, Y. Iwasa, M. Kawasaki, B. Keimer, N. Nagaosa, and Y. Tokura, Nat. Mater. **11**, 103 (2012).

[28] M. Gibert, P. Zubko, R. Scherwitzl, J. Íñiguez, and J.-M. Triscone, Nat. Mater. **11**, 195 (2012).

[29] D. Xiao, W. Zhu, Y. Ran, N. Nagaosa, and S. Okamoto, Nat. Commun. **2**, 596 (2011).

[30] I. Hallsteinsen, M. Moreau, A. Grutter, M. Nord, P.-E. Vullum, D. A. Gilbert, T. Bolstad, J. K. Grepstad, R. Holmestad,

S. M. Selbach, A. T. N'Diaye, B. J. Kirby, E. Arenholz, and T. Tybell, Phys. Rev. B **94**, 201115 (2016).

[31] M. Moreau, A. Marthinsen, S. M. Selbach, and T. Tybell, Phys. Rev. B **95**, 064109 (2017).

[32] R. Søndenå, P. Ravindran, S. Stølen, T. Grande, and M. Hanfland, Phys. Rev. B **74**, 144102 (2006).

[33] T. Negas and R. S. Roth, J. Solid State Chem. **1**, 409 (1970).

[34] T. Takeda and S. Ohara, J. Phys. Soc. Jpn. **37**, 275 (1974).

[35] Y. Syono, S.-iti Akimoto, and K. Kohn, J. Phys. Soc. Jpn. **26**, 993 (1969).

[36] V. F. Balakirev and Y. V. Golikov, Inorg. Mater. **42**, S49 (2006).

[37] J. H. Lee and K. M. Rabe, Phys. Rev. Lett. **104**, 207204 (2010).

[38] R. E. Cohen, Nature (London) **358**, 136 (1992).

[39] J. M. Rondinelli, A. S. Eidelson, and N. A. Spaldin, Phys. Rev. B **79**, 205119 (2009).

[40] G. Kresse and J. Furthmüller, Phys. Rev. B **54**, 11169 (1996).

[41] J. P. Perdew, K. Burke, and M. Ernzerhof, Phys. Rev. Lett. **77**, 3865 (1996).

[42] J. Hong, A. Stroppa, J. Íñiguez, S. Picozzi, and D. Vanderbilt, Phys. Rev. B **85**, 054417 (2012).

[43] P. E. Blöchl, Phys. Rev. B **50**, 17953 (1994).

[44] A. Togo and I. Tanaka, Scr. Mater. **108**, 1 (2015).

[45] H. T. Stokes and D. M. Hatch, J. Appl. Crystallogr. **38**, 237 (2005).

[46] R. D. King-Smith and D. Vanderbilt, Phys. Rev. B **47**, 1651 (1993).

[47] D. Vanderbilt and R. D. King-Smith, Phys. Rev. B **48**, 4442 (1993).

[48] B. Dabrowski, O. Chmaissem, J. Mais, S. Kolesnik, J. D. Jorgensen, and S. Short, J. Solid State Chem. **170**, 154 (2003).

[49] A. Marthinsen, C. Faber, U. Aschauer, N. A. Spaldin, and S. M. Selbach, MRS Commun. **6**, 182 (2016).

[50] R. Oja, K. Johnston, J. Frantti, and R. M. Nieminen, Phys. Rev. B **78**, 094102 (2008).

[51] A. Raeliarijaona and H. Fu, J. Appl. Phys. **115**, 54105 (2014).

[52] See Supplemental Material at http://link.aps.org/supplemental/10.1103/PhysRevMaterials.2.014404 for more about comparison of the energy landscapes of rotational and polar modes with (001) strain and (111) strain, bond lengths as a function of mode amplitude with (001) and (111) strain, decomposed total energy of rotational modes under compressive (111) strain as well as their energy dependence on Hubbard U, energy landscape and density of states of polar modes with FM order under tensile (111) strain, oxygen formation energies with (111) strain, evolution of octahedral rotations with isostatic strain, a derivation of the pseudocubic rotational angles upon compressive strain, and substrate considerations.

[53] S. M. Griffin, M. Lilienblum, K. T. Delaney, Y. Kumagai, M. Fiebig, and N. A. Spaldin, Phys. Rev. X **2**, 041022 (2012).

[54] P. W. Higgs, Phys. Rev. Lett. **13**, 508 (1964).

[55] F. Englert and R. Brout, Phys. Rev. Lett. **13**, 321 (1964).

[56] P. B. Littlewood and C. M. Varma, Phys. Rev. Lett. **47**, 811 (1981).

[57] P. B. Littlewood and C. M. Varma, Phys. Rev. B **26**, 4883 (1982).

[58] M. Moreau, S. M. Selbach, and T. Tybell, arXiv:1710.10996.

[59] C. Ruegg, N. Cavadini, A. Furrer, H.-U. Gudel, K. Kramer, H. Mutka, A. Wildes, K. Habicht, and P. Vorderwisch, Nature (London) **423**, 62 (2003).